COBEM 2023 27TH INTERNATIONAL CONGRESS OF MECHANICAL ENGENEERING

ABCM Brazilian Society of Mechanical Sciences and Engineering
27th ABCM International Congress of Mechanical Engineering
December 04-08, 2023, Florianópolis-SC, Brazil

COB-2023-1074
ANALYSIS OF FATIGUE CRACK GROWTH BEHAVIOR AND THE INFLUENCE OF CORROSION OF ASTM A285C STEEL APPLIED IN KRAFT CONTINUOUS DIGESTER

Alexandre Nakayama
Klabin S.A. – Fazenda Monte Alegre s/n – Telêmaco Borba - Brazil
nakayama@klabin.com.br

André Luiz Moreira de Carvalho
João Paulo Gabre Ferreira
Ponta Grossa State University – Uvaranas Campus – Ponta Grossa - Brazil
andrelmc@uepg.br
joao_gabre@hotmail.com

Abstract. *In the cellulose pulp and paper industry, the cooking process is essential in producing cellulose fibers. This process involves removing lignin and other impurities from wood chips using an alkaline aqueous solution called white liquor under high temperatures and pressures. The continuous digester, a vertical pressure vessel where the cooking takes place, is subjected to a fatigue damage mechanism that is usually only detectable through non-destructive inspections during equipment outages. This paper presents the results of fatigue tests conducted on ASTM A285C steel to investigate the stable crack propagation of the fatigue crack growth (FCG) curves and to evaluate the influence of alkaline corrosion on the fatigue process. Compact tension-type specimens were tested according to ASTM E647-05 in as-received and after-immersion corrosion test conditions. The results showed that, in the early crack growth stage II, the FCG of the as-received specimens had a significantly lower rate than the corroded condition. However, in ΔK over approximately 40 MPa$\sqrt{m}$, the FCG rates of both conditions tend to converge. It was noticed that in the low ΔK region, the corrosion played a role in increasing the growth rate, possibly due to surface damages and the influence on the crack tip conditions.*

Keywords: *fatigue, pressure vessel, Kraft digester, corrosion.*

1. INTRODUCTION

Continuous digesters represent one of the most serious and potentially severe exposures (Rahman et al., 2020) and one of the highest investments in equipment in a cellulose pulp mill (Correia, 2010). Besides the safety hazards, its downtimes have a substantial economic impact since the digester is the main component in the cooking process. Therefore, the structural and operational reliability of the digester is vital importance to maintain its financial lifecycle.

During its delignification operations, i.e., removing lignin and other impurities from wood chips using an alkaline aqueous solution, as well called white liquor composed mainly of NaOH and Na_2S under high temperatures and pressures. It has solid, liquid, and vapor phases in its interior with conditions strongly dependent on heat and mass transport phenomena, besides the evolution of chemical reactions (Paoliello et al., 2011).

The continuous digesters have three distinctive zones during the delignification process: impregnation zone (first contact of the wood chips with the heated white liquor), cooking zone (separation of the lignin from the wood chips to form the cellulose fibers) and washing zone (cellulose fibers separation and residual lignin removal). The main operational parameters are the alkaline load profile along the process keeping the highest level of sulfide ions during the early stages of delignification to protect the carbohydrates from severe degradation and the temperature profile along the digester (Michelsen and Foss, 1996).

Accordingly, these operations produce loads at the digester walls due to variable internal pressure and temperatures. Therefore, fatigue, along with the corrosive environment of the white liquor, is an active damage mechanism (Klarin-Henricson, 2004). In this context, the current work aims to investigate the influence of the corrosive alkaline exposure on fatigue crack growth from ASTM A285C steel specimens, currently used in Kraft continuous digesters.

2. MATERIALS AND METHOD

Compact tension C(T) specimens according to ASTM E647-05 were obtained from an ASTM A285C hot rolled steel plate with 25,4 mm thickness (Figure 1). They were machined by the WEDM process with 0,25 mm diameter wire and

with 20 mm of net thickness B. Regarding the rolling direction of the plate, the 4 C(T) specimens manufactured followed the crack plane orientation T-L as illustrated in Figure 2 (ASTM E399, 2005).

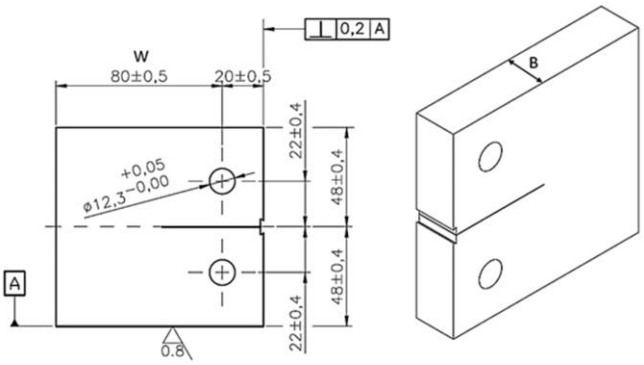

Figure 1. Geometry from the Compact tension C(T) fatigue test specimen (dimension in mm).

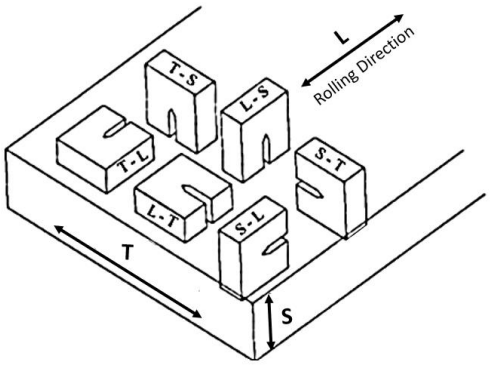

Figure 2. Specimens aligned with crack plane orientation (ASTM E399, 2005).

Two specimens, numbered 1 and 2, were fatigue tested according to ASTM E647-05 standard in the as-received condition and two specimens, numbered 3 and 4, were immersion corrosion tested according to ASTM G31-72 in white liquor extracted from a natural production process before fatigue tests. Sulfidity of the white liquor, the ratio between the sodium sulfide concentration and active alkali as shown in Eq. 1, was 40,5±1,5 % and the liquor temperature controlled to 369±1 K. After the immersion corrosion test, the specimens had the corrosion residues removed in an ultrasonic washer with deionized water and dried with dry compressed air. The corrosion rates were determined with the use of a precision digital scale with 10^{-6} kg readability by weighing the specimens before and after the immersion test according to Eq. 2, where K is a normalized constant, W is the mass loss, A is the superficial specimen area, T is the immersion test time and D is the specimen material density (ASTM G31, 1972).

$$Sulfidity\ (\%) = \frac{Na_2S}{NaOH+Na_2S} \tag{1}$$

$$Corrosion\ rate = (K \cdot W) \cdot (A \cdot T \cdot D) \tag{2}$$

A fatigue pre-crack was introduced in all specimens at room temperature through a sinusoidal waveform load at a frequency of 10 Hz and a stress ratio of 0,1. The fatigue crack propagation tests were obtained with constant amplitude-controlled load and sinusoidal load waveform at a frequency of 10 Hz.

Stress intensity factor ΔK was determined from the crack length measured during the fatigue crack growth test according to Eq. 3, where ΔP is the force range, B is the net specimen thickness, W is the specimen width, and α is the relation between the crack length and the specimen width.

$$\Delta K = \frac{\Delta P}{B\sqrt{W}} \cdot \frac{(2+\alpha)}{(1-\alpha)^{\frac{3}{2}}} \cdot (0{,}866 + 4{,}64\alpha - 13{,}32\alpha^2 + 14{,}72\alpha^3 - 5{,}6\alpha^4) \tag{3}$$

The crack length during the test was measured with the use of a clip gage attached to the specimen as shown in Figure 3 and the compliance method according to Eq. 4 and Eq. 5 where C_1, C_2, C_3, C_4 and C_5 are flexibility coefficients, u_x is the compliance quantity, E is the elastic modulus, v is the displacement between measurements points or the crack opening

displacement COD, and P is the force. Equations 4 and 5 are the analytically derived relationship between compliance, the reciprocal of the force-displacement slope normalized for elastic modulus and specimen thickness, and the crack size for the normalized compact tension C(T) specimen (ASTM E647, 2005).

$$\frac{a}{W} = C_0 + C_1 u_x + C_2 u_x^2 + C_3 u_x^3 + C_4 u_x^4 + C_5 u_x^5 \tag{4}$$

$$u_x = \left[\left(\frac{EvB}{P}\right)^{\frac{1}{2}} + 1\right]^{-1} \tag{5}$$

Figure 3. Clip gage attached to the C(T) specimen.

Fatigue crack growth tests were performed in an MTS Landmark 370.25 machine. After the FCG tests, the specimens were sectioned, and the fracture surface was analyzed in a scanning electron microscope SEM to identify fracture micromechanisms. SEM analyses were performed in a Tescan Mira 3 equipment.

Microstructural characterization was done via Nital etching (2% nitric acid in ethanol) according to ASTM E3-11 by optical microscopy in three samples from the ASTM A285C hot rolled steel plate: normal ND, rolling RD and transversal TD directions, respectively. In each metallographically prepared sample, the general grain size of the structure was measured according to the planimetric procedure of the ASTM E112-10 standard. The fraction of phases measured with the aid of the digital image processing program Image J that, through the distinction in shades of gray of the micrograph associated with phases and constituents, the quantification of the selected area is made.

3. RESULTS AND DISCUSSION

3.1 Microstructural characterization

Figure 4 presents the micrographs from ND, RD and TD directions. The material has a typical hot-rolled structure consisting of a ferrite phase and pearlite constituent, as expected for a hypoeutectoid structural steel. Steels with a ferritic-pearlitic structure, also denominated F-P steels, are used in a wide range of engineering structures due to the combination of high mechanical strength and ductility and this type of F-P microstructure can be considered from the point of view of interaction between two ductile phases (Mao and Liao, 2019).

The micrographs of Figure 4 show a moderately heterogeneous structure in the distribution of constituents and grain size in the ND direction; however, it does not show a significant presence of inclusions. The micrographs of the RD and TD directions show a microstructural banding characterized by the existence of alternating layers of proeutectoid ferrite and pearlite aligned with the direction of the mechanical work imposed on the sheet during its lamination (Thompson and Howell, 1992).

Microstructural banding originates from interdentritic residual microsegregations formed during solidification. The conditions created during the hot rolling of steel in the austenitic condition provide the formation of regions of high concentrations of solutes, and this distribution of solutes provides the basis for microstructural banding. The occurrence and degree of banding are influenced by the austenitic grain size and the cooling conditions during the rolling process that control the austenite decomposition into other phases and constituents (Krauss, 2003).

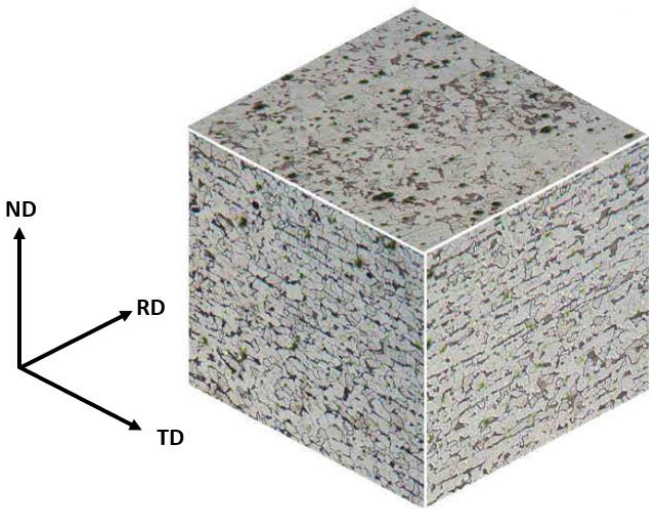

Figure 4. Micrographs from the ND, RD and TD directions of the ASTM A285C.

The grain size of the three directions is equivalent to 34.2 µm of mean diameter. The size and arrangement of microstructural grains are of great relevance in the mechanisms and properties of steel fracture. The strength and toughness of F-P steels also depend on grain texture and shape. In general, grain size reduction can simultaneously increase the strength and toughness of steels (Igwemezie, 2019).

The average volumetric fraction of the ferrite phase in the microstructure is 86.3% measured from the analysis of the micrographs from ND, RD and TD directions. In research using a material with a specification similar to that of this work, Subramanian et al. (2003) and Sindelar et al. (2000) obtained volumetric ferrite fractions of 87.2±3% and 87.4±2.4%, respectively.

3.2 Immersion corrosion tests

The corrosion rate obtained from specimens numbered 3 and 4 after the fatigue pre-cracked, presented in Table 1, is compatible with the environment and material relationship reported in the literature. In research on the effect of sulfide on the corrosivity of white liquor in carbon and stainless steels, Wensley and Champagne (1999) found a corrosion rate of 1.22 mm per year for ASTM A285C steel in an immersion test in white liquor extracted from a production process at 371 K and 84 g/l of NaOH and 55.9 g/l of Na_2S. For a composition of 84 g/l of NaOH and 39 g/l of Na_2S of the white liquor at a temperature of 361 K, Wensley (2004) found a corrosion rate of 0.76 mm per year. The corrosion rate of carbon steels strongly depends on the composition of the white liquor, with concentrations of NaOH and Na_2S playing preponderant roles.

Table 1. Corrosion rate for the specimens T-L orientation

	Corrosion rate (mm/year)
Specimen 3	1,243
Specimen 4	1,268

3.3 Fatigue crack growth tests

Figure 5 presents in bi-logarithmic scale, the stage II or the stable crack propagation, of the FCG tests da/dN in function of ΔK for the specimens tested in as-received (specimens numbered 1 and 2) and after immersion corrosion condition (specimens numbered 3 and 4).

Fatigue crack growth rate is determined by the stress-strain state ahead of the crack. In stage II, the crack growth is associated with the high stress levels that cause cyclic plastic deformation at the crack tip by the Laird-Smith mechanism of blunting and re-sharpening of the crack tip (Vormwald, 2016).

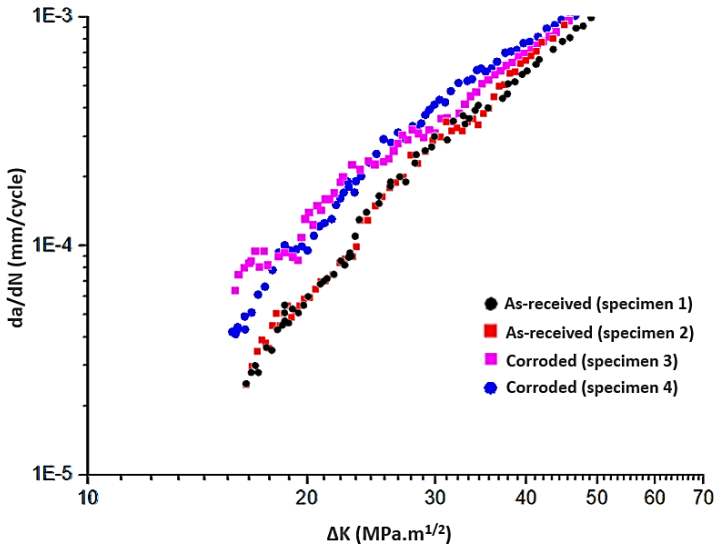

Figure 5. Stable crack propagation da/dN x ΔK curves for the specimen´s T-L orientation in as-received (specimens 1 and 2) and corroded conditions (specimens 3 and 4).

Table 2 shows the values of parameters C and m of the Paris model (represented by Eq. 6) determined by the linear regression curve fit of experimental data. The exponent m is an empirical measure of the slope of the curve in the stable fatigue crack propagation stage of the Paris model, and for the same test conditions, higher values of m indicate favoring crack growth resulting in lower fatigue life. For Dowling (1999), a possible generalization about the exponent m is that materials with low ductility (more brittle) have higher values. For ductile metals, the value of m is typically between 2 and 4 and often around 3.

$$\frac{da}{dN} = C \cdot (\Delta K)^m \tag{6}$$

Table 2. Parameters C and m of the Paris model for specimens 1 to 4.

	C	m
Specimen 1	$2{,}63 \times 10^{-12}$	3,35
Specimen 2	$3{,}34 \times 10^{-12}$	3,27
Specimen 3	$3{,}31 \times 10^{-11}$	2,73
Specimen 4	$1{,}41 \times 10^{-11}$	2,99

In the stable fatigue propagation stage, the crack interacts with the region close to its tip and the distribution of phases, microconstituents and inclusions can affect the propagation rate. As observed in Fig. 4, the pearlite in the ND direction has a networked-like morphology. As illustrated in Fig. 6, the network morphology of pearlite has lower resistance to fatigue crack propagation compared to the distributed morphology. In the distributed morphology, the resistance to propagation is greater due to the crack path with more deflections, occurrence of the crack closure phenomenon and smaller size of the plastic zone at the crack tip (Korda et al., 2007).

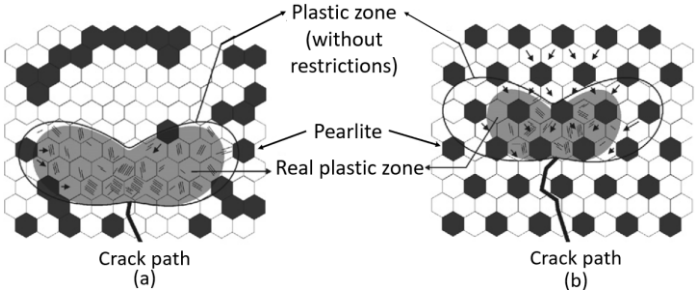

Figure 6. Schematic drawing of the influence of pearlite distribution on the ferritic matrix in the plastic zone in front of the crack. (a) network morphology (b) distributed morphology (Korda et al., 2007).

Regarding the effect of previous corrosion in the fatigue crack growth curves, it is possible to observe that the exponent m of the Paris model for specimens 3 and 4 decreased in relation to specimens 1 and 2 in the as-received condition. One of the effects of previous corrosion was to rotate the crack propagation curve clockwise. This reduction of the exponent m of the Paris model indicates that, as soon as the crack reaches a certain length, an increase of the stress intensity factor ΔK or the load level leads to a deceleration of the fatigue crack propagation rate in part of stage II when compared to the as received condition. Figure 5 illustrates the rotation of the crack propagation curves from the corroded condition in relation to as-received condition, as the values of da/dN gradually decrease from a difference of approximately 49% at ΔK of 20 MPa.m$^{1/2}$ to 15% at ΔK of 40 MPa.m$^{1/2}$. The average FCG curve for the corroded condition rotates around a virtual intersection point located in ΔK value where the crack advance per cycle is practically the same for both conditions.

Over a ΔK range of approximately 15 to 40 MPa.m$^{1/2}$, during a substantial portion of stage II, the as-received fatigue crack propagation rate in both specimens 1 and 2 is significantly lower than the rate of specimens in the condition after the white liquor immersion corrosion test. Knysh et al. (2019) and Palin-Luc et al. (2010) observed similar results of higher fatigue crack growth rates after corrosion conditions.

The FCGR curves tend to converge in a ΔK of approximately 45 MPa.m$^{1/2}$. Table 3 shows fatigue crack propagation rate da/dN value in mm per cycle corresponding to ΔK values of 20, 25, 30, 35 and 40 for as-received conditions (specimens 1 and 2) and after-immersion corrosion test in white liquor (specimens 3 and 4).

Table 3. Crack propagation rate in mm/cycle for values of ΔK in stage II.

	ΔK (MPa.m$^{1/2}$)				
	20	**25**	**30**	**35**	**40**
Specimen 1	5,95x10^{-5}	1,57x10^{-4}	2,95x10^{-4}	4,05x10^{-4}	6,65x10^{-4}
Specimen 2	5,75x10^{-5}	1,53x10^{-4}	2,75x10^{-4}	4,03x10^{-4}	5,86x10^{-4}
Specimen 3	1,35x10^{-4}	2,31x10^{-4}	3,35x10^{-4}	5,21x10^{-4}	7,05x10^{-4}
Specimen 4	9,51x10^{-5}	2,73x10^{-4}	4,25x10^{-4}	5,72x10^{-4}	7,71x10^{-4}

According to Igwemezie (2019), another relevant information suggested from the clockwise rotation of the fatigue crack propagation curve due to corrosion effects is that the limit value or threshold of the stress intensity factor ΔK_{th} variation is greater for the as-received condition. Corrosion is a factor that affects fatigue crack growth and the da/dN curve as a function of ΔK tends to shift to the left (or rotate clockwise) the greater the effect of corrosion. In most systems with metal and corrosive media interaction, the crack propagation rate increases relative to the propagation rate in the absence of corrosion effects (Oliveira, 2008).

3.4 Fatigue fracture surface analysis

To analyze the fatigue fracture mechanism, fracture surface and crack morphology were observed and characterized at the micro level. SEM images at different magnifications taken from the fracture surfaces of fatigue tests of as-received specimens are shown in Figure 7. Micrograph images from fatigue tests of after-immersion corrosion specimens are shown in Figure 8. The direction of fatigue crack propagation for all SEM images is from left to right.

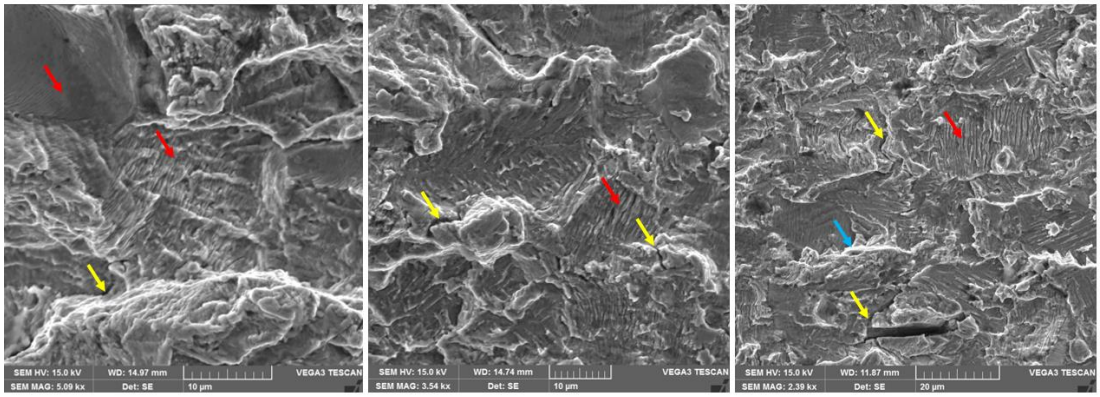

Figure 7. Fractography of fatigue crack propagation of as-received condition specimen.
(a) ΔK ≈ 20 MPa.m$^{1/2}$ (b) ΔK ≈ 30 MPa.m$^{1/2}$ (c) ΔK ≈ 45 MPa.m$^{1/2}$.

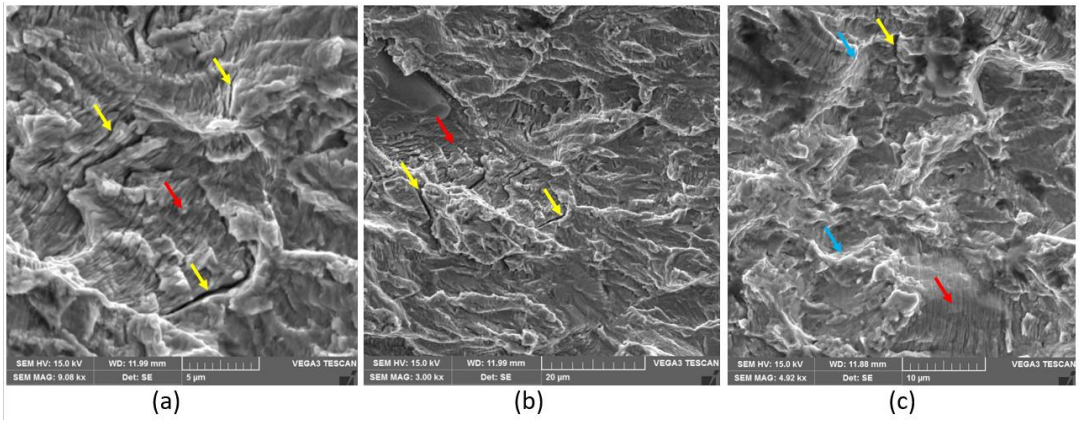

Figure 8. Fractography of fatigue crack propagation of after immersion corrosion condition specimen. (a) $\Delta K \approx 20$ MPa.m$^{1/2}$ (b) $\Delta K \approx 30$ MPa.m$^{1/2}$ (c) $\Delta K \approx 45$ MPa.m$^{1/2}$.

Figures 7 and 8 show the typical characteristics of striations in the fatigue crack growth mechanism in the crack-expanding region. Red arrows indicate the morphological feature of ductile striations mechanism DSM. According to Ritchie (1999) and Zhu et al. (2021), fatigue failure in metals is generally characterized by a transgranular ductile striation mechanism DSM. Such striations represent local crack-growth increments and have been hypothesized to occur via the mechanism of opening and blunting the crack tip on loading, followed by resharpening of the tip on unloading, the well-known Laird-Smith model. Several theoretical models for stage II of fatigue crack growth rely on the fact that where plastic zones are sufficiently large compared to microstructural dimensions, plastic blunting at the crack tip is accommodated by shear on two slip-systems approximately 45º to the crack plane. A new crack surface can be created during cyclic crack advance either by simultaneous or alternating slip on two slip systems.

Secondary cracking SC indicated by yellow arrows in Figures 7 and 8 are observed on both as-received and after-corrosion immersion conditions. SC mechanism, according to Bai (1988), can be attributed to the facts that some micro-cracks may initiate along the blunted border of the crack for the local high-tension stress existing, especially if there are grain or sub-grain boundaries and other defects in the material matrix, and that if inclusion or defect satisfy the condition to void nucleation, secondary cracking is formed spatially by stress increase due to the presence of void or stress concentration. These two facts imply that SC may occur anywhere there are micro-stress risers and material defects during fatigue crack propagation, especially at sites where the stress state is favorable. The slightly higher incidence of SC in the lower ΔK region (range approximately 20 to 25 MPa.m$^{1/2}$) after-immersion corrosion condition may be attributed to surface alterations imposed by white liquor corrosivity. The SC occurrences tend to decrease the m values of the Paris model for after corrosion-immersion specimens as seen in Figure 5 but with higher crack growth rate da/dN in most of stage II compared with the as-received condition.

Tearing ridges indicated by blue arrows in Figures 7 and 8 suggest a large stress concentration at the fatigue crack tip and the crack propagation was prone to deflection under normal stress (Zhu et al., 2021). According to Millela (2012), striations are grouped in areas of homogenous propagation separated by tear ridges in which material fails by shearing resulting in the apparent continuity of the fatigue advancing front.

4. CONCLUSIONS

Based on the tests performed in the present work, the following conclusions can be drawn:

- Fatigue crack growth is not sensitive by the microstructural ferrite-perlite banding observed in the RD (rolling direction) and TD (transverse direction) for T-L specimens.
- The pre-corroded specimens showed approximately 49% higher crack propagation rate in the low ΔK region than in as-received conditions. It is likely due to the surface damage caused by the corrosion process and its influence on the conditions at the crack tip. At higher ΔK regions, the effect of pre-existing corrosion on the crack growth rate diminishes, and the behavior of the two conditions becomes more similar.
- SEM fatigue fracture surface results show that in the after-immersion-corrosion conditions, there were slightly higher occurrences of secondary cracks in the lower ΔK region. These secondary cracks likely contributed to a lower fatigue crack propagation rate than the as-received specimens.

5. REFERENCES

American Society for Testing and Materials, 2011. “Standard guide for preparation of metallographic specimens”. ASTM E3-11.

American Society for Testing and Materials, 2005. “Standard test method for linear-elastic plane-strain fracture toughness of metallic materials”. ASTM E399-05.

American Society for Testing and Materials, 2005. “Standard test method for measurement of fatigue crack growth rates”. ASTM E647-05.

American Society for Testing and Materials, 1972. “Standard guide for laboratory immersion corrosion testing of metals”. ASTM G31-72.

Bai, J.B., Chen, Y.S., 1988. Secondary crack during surface crack growth under tensile fatigue loading, Engineering Fracture Mechanics, Vol. 30, pp. 167-168.

Correia, F.M., 2010. *Analysis of compactation disturbance of eucalyptus chips in vapor phase digester (in Portuguese).* Master´s dissertation, Graduate Program in Engineering, Viçosa Federal University, Viçosa, Brazil.

Dowling, N.E., 1999. *Mechanical behavior of materials*. Pearson Publishing, Essex.

Igwemezie, V., Dirisu, P., Mehmanparast, A., 2019. Critical assessment of the fatigue crack growth rate sensitivity to material microstructure in ferrite-pearlite steels in air and marine environment, Materials Science & Engineering A, Vol. 754, pp. 750-765.

Klarin-Henricson, A., 2004. Corrosivity of liquors in continuous digesters, TAPPI Journal, Vol. 3, pp. 13-18.

Korda, A.A., Miyashita, Y., Mutoh, Y., Sadasue, T., 2007. Fatigue crack growth behavior in ferritic-pearlitic steels with networked and distributed pearlite structure, International Journal of Fatigue, Vol. 29, pp. 1140-1148.

Knysh, V., Solovie, S., Nyrkova, L., Klochkov, I., Motrunich, S., 2019. Influence of the atmosphere corrosion on the fatigue life of welded T-joints treated by high frequency mechanical impact, Procedia Structural Integrity, Vol. 16, pp. 73-80.

Krauss, G., 2003. Solidification, segregation and banding in carbon and alloy steels, Metallurgical and Materials Transactions B, Vol. 34B, pp.781-792.

Mao, B., Liao, Y., 2019. Modelling of lüders elongation and work hardening behaviors of ferrite-pearlite dual phase steels under tension, Mechanics of Materials, Vol. 129, pp. 222-229.

Michelsen, F.A., Foss. B.A., 1996. A dynamic model of the interaction between the chemical reactions and the residence time in a continuous digester, TAPPI Journal, Vol. 79, pp. 170-176.

Millela, P.P., 2012. *Fatigue and corrosion in metals*. Springer Publishing, Milano.

Oliveira, L.G., 2008. *Determination of the fatigue crack growth rate of the steels SAE1050 and SAE4130 used in the production of railway shafts (in Portuguese).* Master´s dissertation. Graduate Program in Mechanical Engineering, Paulista State University, Guaratingueta, Brazil.

Palin-Luc, T., Perez-Mora, R., Bathias, C., Domínguez, G., Paris., P.C., Arana, J.L., 2010. Fatigue crack initiation and growth on a steel in the very high cycle regime with sea water corrosion, Engineering Fracture Mechanics, Vol. 77, pp. 1953-1962.

Paoliello, F.A., Lins, V.F.C., Cardoso, M., 2011. Influence of cooking conditions on continuous digester corrosion in a Brazilian pulp mill, TAPPI Journal, pp. 51-80.

Rahman, M., Avelin, A., Kyprianidis, K., 2020. A review on the modeling, control and diagnostics of continuous pulp digesters, Processes, Vol. 8, pp. 1231-1257.

Ritchie, R.O., 1999. Mechanisms of fatigue-crack propagation in ductile and brittle solids, International Journal of Fracture, Vol. 100, pp. 55-83.

Sindelar, R.L., Lam, P.S., Caskey, G.R., 2000. “Mechanical properties for fracture analysis of mild steels storage tanks”. *In Proceedings of ASME Pressure Vessels and Piping Conference – PVP2000.* Seattle, USA.

Subramanian, K.H., Wiersma, B.J., Duncan, A.J., Harris, S.P., 2003. “Statistical model for prediction of plate-specific fracture toughness properties of ASTM A285 steel”. *In Proceedings of ASME Pressure Vessels and Piping Conference – PVP2003.* Cleveland, USA.

Thompson, S.W., Howell, P.R., 1992. Factors influencing ferrite/pearlite banding and origin of large pearlite nodules in a hypoeutectoid plate steel, Materials Science and Technology, Vol. 8, pp. 777-784.

Vormwald, M., 2016. Effect of cyclic plastic strain on fatigue crack growth, International Journal of Fatigue, Vol, 142, pp. 120-129.

Wensley, A., Champagne, P., 1999.Effect of sulfidity on the corrosivity of white, green and black liquors. In *Proceeding of National Association of Corrosion Engineers Conference – NACE 1999*. San Antonio, USA.

Wensley, A., 2004. Corrosion in alkaline pulping liquors”. In *Proceeding of National Association of Corrosion Engineers Conference – NACE 2004*. New Orleans, USA.

Zhu, Q., Zhang, P., Peng, X., Yan, L., Li, G., 2021. Fatigue crack growth behavior and fracture toughness of EH36 TMCP steel, Materials, Vol. 14, pp. 6621-6639.

6. RESPONSIBILITY NOTICE

The authors are the only ones responsible for the printed material included in this paper.